

# Mechanical properties of chiral actin filaments

Amir Khosravanzadeh\* and Serge Dmitrieff†

*Université Paris Cité, CNRS, Institut Jacques Monod, F-75013 Paris, France*

François Nédélec

*Sainsbury Laboratory, University of Cambridge, Cambridge, United Kingdom*

(Dated: January 1, 2026)

The mechanical properties of actin filaments are essential to their biological functions. Here, we introduce a highly coarse-grained model of actin filaments that preserves helicity and chirality while enabling mesoscale simulations. The framework is implemented in Cytosim, an open-source cytoskeleton simulation platform. We can predict and finely control the shape and mechanical properties of this helical filament, that can be matched to experimental values. Using this model, we investigated the role of filament chirality in motor-driven dynamics. We first show that in two different experimental configurations, motor movement along a helical filament results in a chiral motion of the filament. In a bundle of helical filaments, dimeric motors exert torques on each filament, inducing collective behaviors in the bundle such as rotation, coiling, and helical buckling, reminiscent of those observed in filopodia. Together, these results demonstrate the central role of helicity and chirality in actin mechanics and motor-driven dynamics, and establish our framework as a powerful tool for mesoscale simulations. This framework can also be used for other helical filaments beyond actin.

## I. INTRODUCTION

Actin is one of the fundamental cytoskeletal filaments, playing crucial roles in diverse cellular processes involving cell shape, remodeling and mechanical stability: motility and migration, endocytosis, cell division, morphogenesis, mechanosensitivity, and intracellular transport [1–7]. Actin filaments (F-actin) are right-handed double helices assembled from globular actin (G-actin) monomers [8, 9], making them intrinsically chiral structures. Actin filaments have a radius ( $R$ ) of  $\sim 3$  nanometers and a helical pitch ( $P$ ) of approximately 72 nm [9]. Actin is highly dynamic and continuously undergoes growth, shrinkage, or branching through regulators such as the Arp2/3 complex [10–12]. These dynamic behaviors occur on timescales ranging from nanoseconds to microseconds [13], while filament lengths can extend to several micrometers.

Because of its complexity, actin has been studied extensively using both theoretical models [14–18] and computational simulations [3, 13, 19–21] to investigate its mechanics and dynamics from the molecular to the cell scale. Modeling approaches span a wide range of molecular detail and temporal resolutions, from fully atomistic simulations [22–24] to coarse-grained representations [13, 21, 25, 26], brownian dynamics [27, 28], stochastic-growth models [29], and mean-field or elastic network methods [30–32]. Atomistic simulations capture molecular detail with high accuracy, but they are inherently limited to short length and time scales [19, 22–24]. Coarse-graining reduces atomic details by retaining

only the most relevant degrees of freedom, thereby enabling simulations at larger spatial and temporal scales. [21, 25, 33–36]. The coarse-graining process can be extended to the highest level, in which actin is modeled as a linear filament. Current studies of filament networks rely on such highly coarse-grained representations [37–40], but these models fail to capture essential features such as helicity and chirality. Thus, an intermediate framework in which the filaments retain their chirality is missing.

The functions of actin filaments in-vivo are highly linked to their mechanical properties. Experimental studies have characterized bending persistence length, torsional rigidity, and Young's modulus of the actin filaments [41–43]. The bending persistence length of F-actin ranges from 2 to 17  $\mu\text{m}$  depending on the presence or lack of regulatory proteins [44, 45], while its torsional rigidity is approximately  $8 \times 10^{-26} \text{ Nm}^2$  [46–49], and its Young's modulus is reported to be in the range of a few gigapascal [41, 44, 50]. Here, we seek to build a simulation framework for actin in which it is possible to add these mechanical properties, as well as other actin-associated molecules, including motors, to model the dynamics of actin networks [51].

Myosin motors consume ATP to move along actin filaments, transporting cargo from one end to the other. Because actin filaments are highly elongated helices with pitch-to-radius ratio  $P/R \sim 10$  [9], motor activity is often described purely as translational motion along the filament. However, several single-filament experiments have shown that myosin motors also rotate around the filament as they progress along it [52–59]. Furthermore, networks of actin filaments can exhibit emergent chiral behaviors at the macroscopic scale, which are thought to originate from filament helicity and chirality [60–65]. Yet, because of the complexity of living cells and the

\* amir.khosravanzadeh@ijm.fr

† serge.dmitrieff@ijm.fr

limited resolution of experimental techniques, identifying the microscopic origins of these behaviors remains challenging.

In this study, we introduce a coarse-grained model of actin filaments that preserves their helicity and chirality while enabling simulations at the network scale. We first implement a single isolated helical actin filament, showing that we can use simple models to understand its geometrical and mechanical properties. We then consider a single filament gliding on a bed of motors and recover the chiral rotation as observed in experiments. In the same setup, we show that anchoring the filament minus end results in the filament to spiral clockwise. We then simulate a bundle of filaments connected by dimeric motors, and show that this leads to collective dynamical regimes such as rotation, coiling, and helical buckling, reminiscent of those observed in filopodia, an essential actin-based cellular structure.

## II. MODEL

The simulations in this study present a highly coarse-grained model of actin filaments, enabling the investigation of large-scale filament dynamics over long timescales. To construct the double helical actin filament, we use Cytosim, an open-source simulation platform based on overdamped Langevin dynamics[37]. Cytosim is particularly suitable for modeling large systems of linear, flexible filaments and their interactions with associated proteins, such as molecular motors, diffusible crosslinkers, and nucleators.[66–70]. These filaments are polar, with directionality along their length, and can polymerize or depolymerize at both ends.

To construct a helical filament, we employ two flexible, linear filaments already available in Cytosim. The

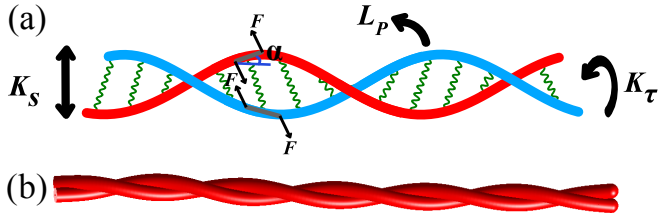


FIG. 1. (a) Schematic representation of a helical actin filament. The filament consists of two linear, flexible protofilaments, each discretized to a series of segments. The two protofilaments are interconnected by a series of springs. A torque,  $\Gamma$ , applied to each pair of facing segments induces a twist that transforms the whole structure into a double-helical filament. This torque is implemented as four equal forces acting at the ends of each segment in opposite directions. The mechanical behavior of the helical filament is characterized by three main mechanical properties: torsional rigidity ( $K_T$ ), bending persistence length ( $L_P$ ), and inter-protofilament separation rigidity ( $K_S$ ). (b) Snapshot of the helical filament obtained from Cytosim simulations.

bending energy per unit length of each protofilament is given by  $\frac{1}{2}\kappa C^2$ , where  $C$  is the curvature and  $\kappa$  denotes the bending rigidity of the protofilament. Each protofilament is composed of a discretized chain of vertices separated by a fixed distance  $ds$ , referred to as the segmentation length. Every two segments facing each other are linked by a spring, as illustrated in Fig. 1. The energy of a single spring is described by  $\frac{1}{2}K(R - R_0)^2$ , where  $K$  is the spring stiffness,  $R$  is the instantaneous distance between the two protofilaments (helix radius), and  $R_0$  is the resting length. Each pair of opposing protofilament segments, connected by a spring, is subjected to a torque  $\Gamma$ , which induces a twist and converts the structure into a double helix. This torque is implemented as four equal forces applied at the segments edges in opposite directions (see Fig. 1). The associated torsional energy is given by  $\frac{1}{2}\Gamma(2\alpha - 2\alpha_0)^2$ , where  $\Gamma$  is the torque stiffness and  $\alpha$  is the angle between each segment and the central axis of the helix (Fig. 1). The angle  $\alpha$  is related to the pitch  $P$  and radius  $R$  of the helix as  $\alpha = \arctan(R/P) \rightarrow R/P$  as  $R \ll P$ .

In the literature such helices are often described using the Frenet-Serret formalism. Briefly, at each vertex  $i$ , a local frame  $\mathbf{F}_i = (\mathbf{t}_i, \mathbf{n}_i, \mathbf{b}_i)$ , is constructed using the following equations:

$$\mathbf{t}_i = \frac{\mathbf{r}_{i+1} - \mathbf{r}_i}{ds}, \quad \mathbf{b}_i = \frac{\mathbf{t}_{i-1} \times \mathbf{t}_i}{|\mathbf{t}_{i-1} \times \mathbf{t}_i|}, \quad \mathbf{n}_i = \mathbf{b}_i \times \mathbf{t}_i, \quad (1)$$

where  $\mathbf{r}_i$  denotes the position vector of the  $i$ th vertex and  $\mathbf{t}_i$ ,  $\mathbf{n}_i$ , and  $\mathbf{b}_i$  represent the tangent, normal, and binormal unit vectors, respectively[71–73]. Two consecutive frames satisfy the recursive relation  $\mathbf{F}_i = \mathbf{F}_{i-1}\mathbf{R}_i$ , where  $\mathbf{R}_i$  is the rotation matrix obtained from the composition of two rotations : one rotation around  $\mathbf{t}_{i-1}$  followed by one rotation about  $\mathbf{b}_{i-1}$ .

While this approach can be useful, in particular to measure fluctuations of long filaments (see supplementary information), in this article, we mostly used the *natural* frame for a double helix :  $\mathbf{t}_i, \mathbf{u}_i, \mathbf{v}_i$ , in which  $\mathbf{u}_i$  is the normalized vector separating the two protofilaments at vertex  $i$  and  $\mathbf{v}_i = \mathbf{u}_i \times \mathbf{t}_i$ . Within both formalisms, the local curvature of the helices,  $C_i$ , can be written as  $C_i = \left| \frac{\partial \mathbf{t}_i(s)}{\partial s} \right| = \|\mathbf{t}_i - \mathbf{t}_{i-1}\|/ds$ .

Assuming curvature  $C$ , pitch  $P$  and radius  $R$  to be constant along the filament arclength, the total energy per unit length of the whole structure can be written as

$$\frac{E(R, P)}{L} = 2\frac{1}{2}\kappa C^2 + 2\frac{1}{2}\rho K(R - R_0)^2 + 2\rho\Gamma(\alpha - \alpha_0)^2, \quad (2)$$

where  $\rho$  is the density of springs, defined as the number of springs per unit length of the helix,  $\rho = N/L = 1/ds$ . In general, the system is characterized by five microscopic parameters:  $R_0$  (initial radius),  $P_0$  (initial pitch),  $\kappa$  (protofilament bending rigidity),  $K$  (springs stiffness), and  $\Gamma$  (torque stiffness). From the total interactions, one obtains an effective helix described by five corresponding macroscopic observables:  $R$  (effective radius),  $P$  (effective pitch),  $L_P$  (helix persistence length),  $K_T$  (helix

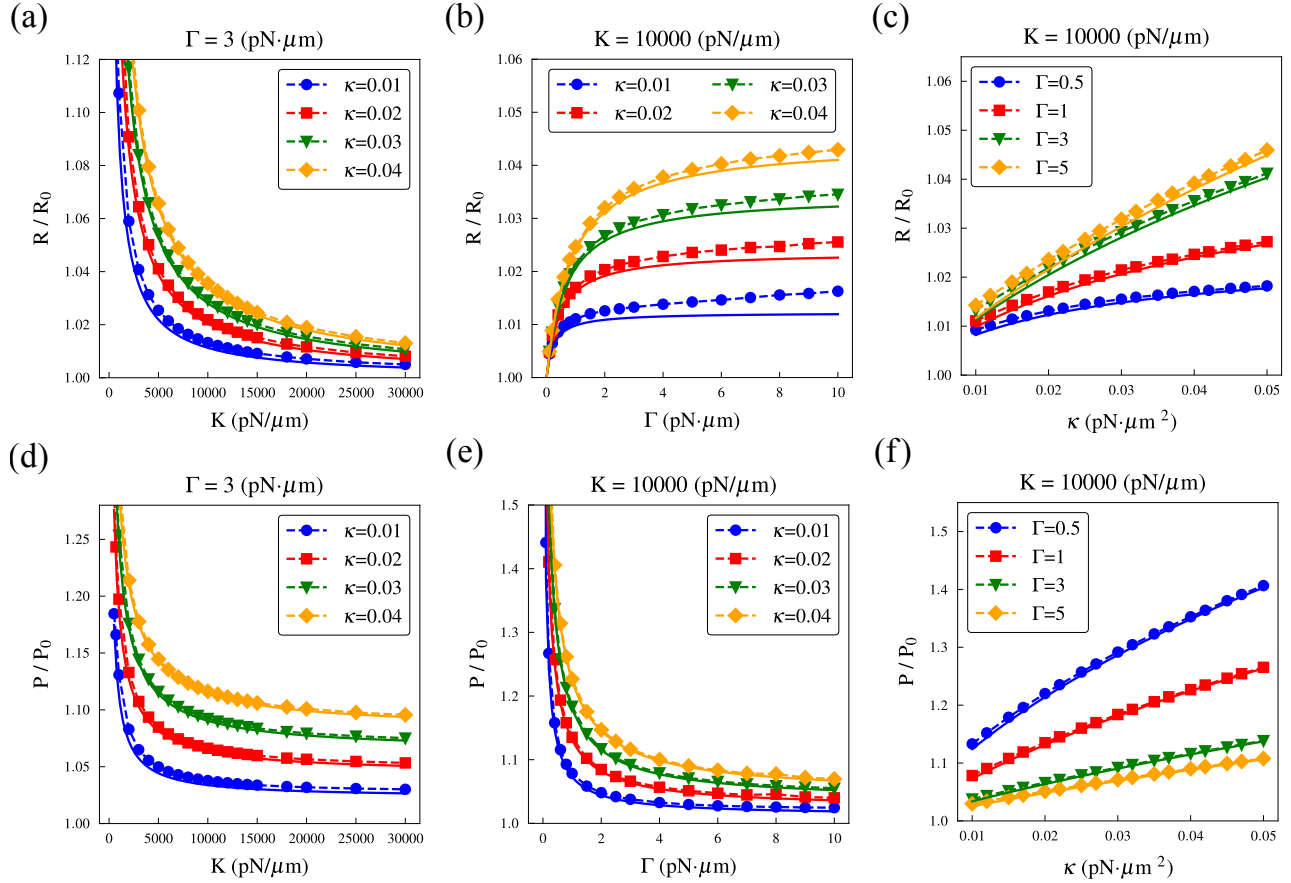


FIG. 2. Variation of normalized radius  $R/R_0$  as a function of (a) spring stiffness  $K$ , (b) torque stiffness  $\Gamma$ , and (c) bending rigidity of the protofilaments  $\kappa$ . Symbols represent simulation results, while solid lines correspond to theoretical predictions from the total energy minimization (Eq. 2). Panels (d-f) show the corresponding variation of normalized pitch  $P/P_0$  as a function of  $K$ ,  $\Gamma$ , and  $\kappa$ , respectively.

torsional rigidity),  $K_s$  (separation rigidity between two protofilaments which is related to the helix Young's modulus). These effective parameters should reproduce experimental values. In the results section, we systematically explore how the macroscopic observables depend on the microscopic inputs.

$$\begin{pmatrix} R_0 \\ P_0 \\ \kappa \\ K \\ \Gamma \end{pmatrix} \iff \begin{pmatrix} R \\ P \\ L_P \\ K_\tau \\ K_s \end{pmatrix}$$

### III. RESULTS

#### A. Geometrical properties of helical filaments

We can predict the helix geometry as a function of the parameters by minimizing numerically Eq. 2 with respect to  $R$  and  $P$ . Qualitatively, we expect  $R$  and  $P$  to be

larger than  $R_0$  and  $P_0$  because the bending energy tends to minimize the curvature. However,  $R$  should approach  $R_0$  when  $K \rightarrow +\infty$  and  $P$  should approach  $P_0$  when  $\Gamma \rightarrow +\infty$ , while  $R/R_0$  and  $P/P_0$  should increase with  $\kappa$ .

This is indeed what we find in our simulations of a helical filaments, Fig. 2. Simulations results closely follow the minimum of the total energy, thus validating our numerical simulation, even at finite temperature.

#### B. Mechanical properties of helical filaments

The mechanics of helical filaments has rightfully attracted considerable attention. However, the system described by Eq. 2 does not map to any analytical model, to the best of our knowledge. Therefore, we decided to directly measure from simulations its mechanical properties as a function of the parameters. To measure the bending persistence length of the helical actin filament, we define a hypothetical backbone by averaging the coordinates of the two protofilaments at each contour position

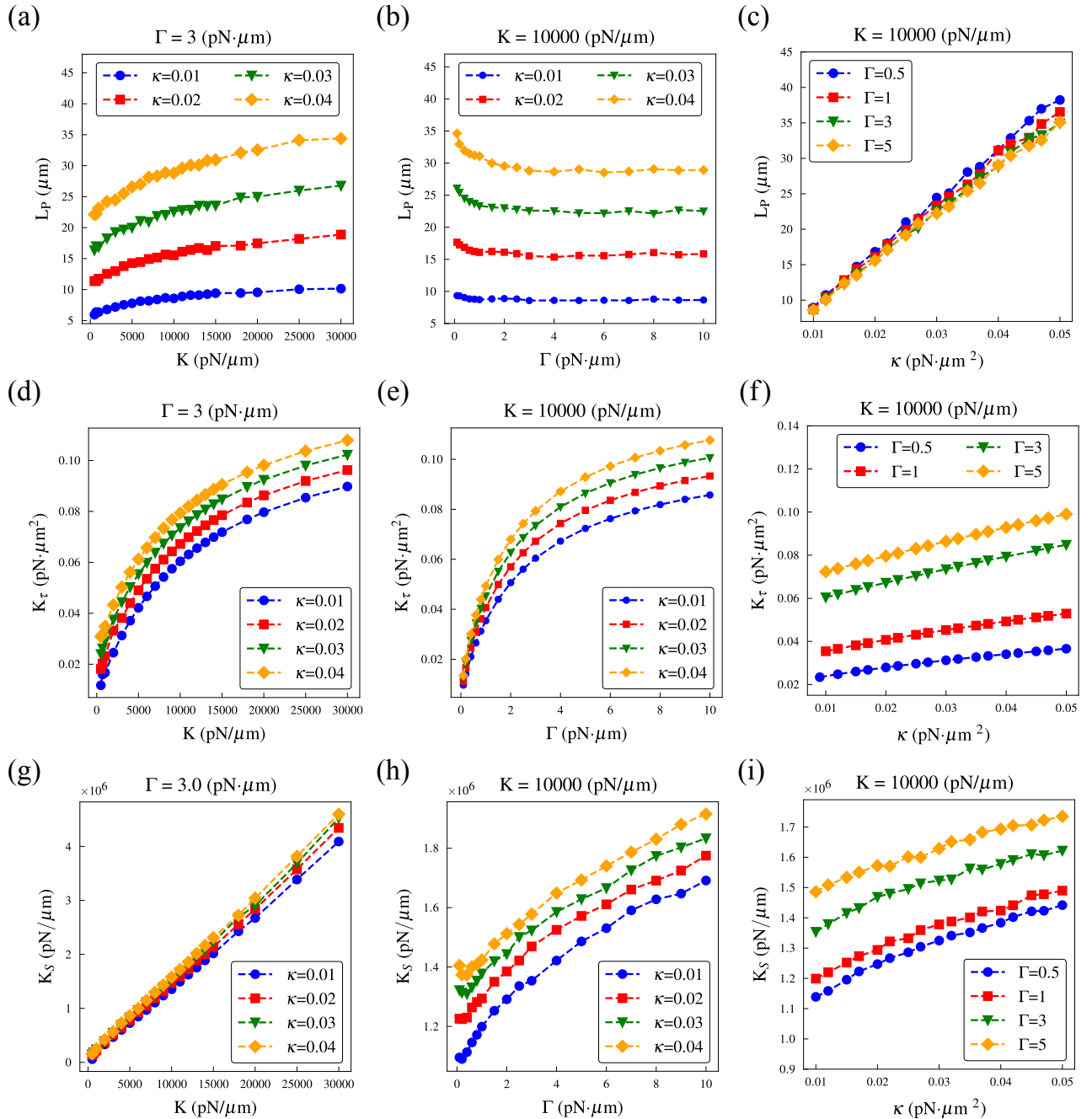


FIG. 3. Effect of (a) spring stiffness  $K$ , (b) torque stiffness  $\Gamma$ , and (c) protofilament bending rigidity  $\kappa$  on the bending persistence length  $L_P$  of the helical filament. Panels (d–f) show the corresponding effect of these parameters on the torsional rigidity  $K_\tau$ . (g) inter-protofilament separation rigidity  $K_S$  as a function of spring stiffness  $K$ , (h) torque stiffness  $\Gamma$ , and (i) protofilament bending rigidity  $\kappa$ . The order of magnitude of  $K_S$  is  $10^6$ , corresponding to a Young's modulus of roughly 1 GPa for the helical filament.

(dashed blue line in Fig. S.2-b). This backbone is a linear structure, and the bending persistence length  $L_P$ , can be obtained from the tangent–tangent correlation function:

$$\langle \mathbf{t}_i \cdot \mathbf{t}_{i+s} \rangle = e^{-s/L_P}, \quad (3)$$

where  $s$  is the contour length along the backbone and  $\mathbf{t}_i$  denotes the unit tangent vector at position  $i$ . A typical measurement of this method is represented in Fig. S.2-a.

We find that the persistence length  $L_p$  is increased near-linearly by increasing protofilament rigidity  $\kappa$ , and increases with spring stiffness  $K$ , as expected from a bun-

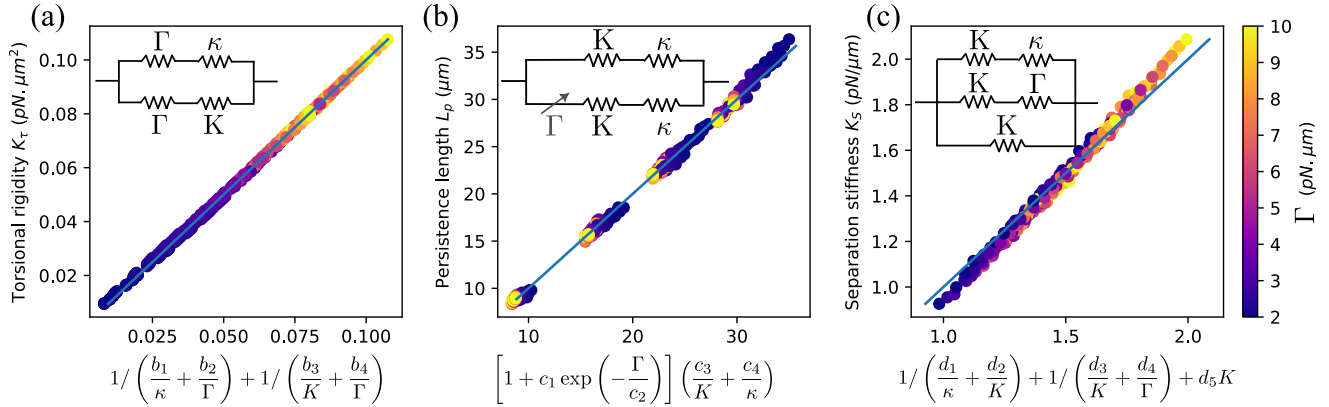


FIG. 4. Minimal models of helix mechanical properties. (a) torsional rigidity behaves as two coupled (in parallel) springs of two independent modes (in series). (b) persistence length behaves as two modes coupled by torsional rigidity ; each mode is made of two independent modes, both controlled by bending rigidity  $\kappa$  and spring stiffness  $K$ . (c) separation stiffness behaves as three coupled units, one of them being pure spring stiffness  $K$ , and the two others being spring stiffness or bending/torsional rigidity.

dle of linear filaments [74]. The persistence length shows a substantial decay for small  $\Gamma$ , while becoming nearly constant for large enough torques. According to the literature [71], the bending rigidity of the helix remains unaffected by the torque, as observed in the latter part. The decaying part can be understood by the behavior of the pitch in the small ranges of  $\Gamma$  (Fig. 2) : at small  $\Gamma$ , the pitch increases and the filament gets closer to a ladder structure. A ladder is much easier to bend in one direction than in the other; analogous to DNA, that can be bent easier in the major grooves than the minor ones [75, 76]. Therefore when  $\Gamma \rightarrow 0$ , one mode of helix fluctuation is suppressed and the persistence length increases.

We then measured the torsional rigidity  $K_\tau$  of the helical filament using a mechanical approach inspired by experiments [46, 48]. In these studies, one end of an actin filament is fixed to a coverslip to constrain both its position and orientation, while the other end is attached to a bead containing fluorescent markers. Holding the bead in an optical trap suppresses bending, and torsional rigidity can be extracted from its rotational diffusion. More recently, magnetic tweezers have been used to apply direct torque to the bead and measure the resulting twist [48]. Following this principle, we applied two equal and opposite torques to the free ends of the helical filament (corresponding to four forces at the protofilaments ends). To prevent bending during twisting, the protofilament ends were fixed in space (black lines in Fig. S.1). As shown in Fig. S.2-c, the rotation response is linear for small applied torques. The torsional rigidity was therefore calculated from the torque-twist relation  $K_\tau = \frac{Tl_0}{\Delta\gamma}$ , where  $T$  is the applied torque,  $l_0$  the initial filament length, and  $\Delta\gamma$  the resulting azimuthal rotation angle. Using this approach, we find that all three rigidities  $K, \kappa, \gamma$  contribute to the helix torsional rigidity  $K_\tau$ .

Next, we measure the distance between protofilaments

to compute an effective separation stiffness  $K_s$  :

$$\frac{1}{2}K_s <(R - \langle R \rangle)^2> = \frac{1}{2}k_B T \quad (4)$$

We find that the separation rigidity  $K_s$  increases near-linearly with the spring stiffness  $K$ , and also increases with  $\Gamma$  and  $\kappa$ , Fig. 3. Our measurements show that the order of magnitude of  $K_s$  is in the range of  $10^6 \text{ pN}/\mu\text{m}$ . Dividing it by the radius of the helix (a few nanometers) yields a Young's modulus  $\sim 1 \text{ GPa}$  for the filament, in agreement with experiments [41, 44, 50, 77].

We then wondered if a simple model could account for these observations. We first focused on the simpler case of torsional rigidity  $K_\tau$  that increases with  $K, \kappa, \Gamma$ . This increase seem to saturate, hinting that there are independent deformation modes : if one stiffness becomes too large, the deformation can be borne by the other stiffnesses. In a minimal model, this corresponds to springs in parallel. We find that the simplest minimal mechanical model consistent with the numerical results is composed of two coupled (in parallel) modes of deformation, made of two independent modes (in series), Fig. 4-a.

We devised a similar model for the persistence length. We expect two bending modes that are coupled by the torque stiffness  $\Gamma$ . These can be modeled as two modes in parallel in which the torsion acts as a variator. Each mode is made of two independent modes assigned to the bending rigidity  $\kappa$  and the spring stiffness  $K$ . Assuming the coupling to decrease exponentially with  $\Gamma$ , we find that this simple model predicts very well simulation results, Fig. 4-b. Lastly, we find that the separation stiffness can also be seen as the sum of three elastic elements in parallel, one of them being a spring with stiffness  $K$ , fig 4-c.

In summary, we established a numerical implementation of a helical filament, that can be quantitatively mapped to a simple geometrical and mechanical model. With adequate microscopic parameters, we therefore can

Symbol	Parameter	value
$\kappa$	Profilaments bending rigidity	$0.02 \text{ pN} \cdot \mu\text{m}^2$
K	Spring stiffness	$10000 \text{ pN}/\mu\text{m}$
$\Gamma$	Torque stiffness	$7 \text{ pN} \cdot \mu\text{m}$
$R_0$	Initial radius	$3 \text{ nm}$
$P_0$	Initial Pitch	$72 \text{ nm}$

TABLE I. Microscopic parameters used to construct the effective helix employed throughout the rest of the paper.

reach values of geometrical and mechanical parameters that fall within the experimentally observed ranges. Different sets of microscopic parameters may be selected to reproduce specific macroscopic properties of different actin filaments or even other helical filaments such as FtsZ, MreB, ParM, SopA, etc[78]. For the remainder of this paper, we adopt the parameter set for the helical actin filament presented in Table I, yielding an actin filament with a persistence length of  $L_p = 15, 75 \mu\text{m}$ , torsional rigidity of  $K_\tau = 8.6 \times 10^{-26} \text{ Nm}^2$ , and a Young's modulus of 0.5 GPa, which are consistent with experimental observations. Having established this model, we can now use it to understand the consequences of the chiral, helical nature of actin.

### C. Actin chirality and its application

#### 1. gliding assay

To reveal the influence of actin helicity on the interaction with motors, we examined the helical filament in a gliding assay, in which filaments are placed on a motor lawn (Fig. 5-a). These motors have a head that can bind anywhere on the filament within a binding range  $r_b$ , at a constant binding rate,  $\omega_{on}$ . Motors are anchored to the substrate by Hookean springs with stiffness  $k_m$  yielding a force  $\mathbf{f}$  given by Hooke's law:  $\mathbf{f} = -k_m(\mathbf{h} - \mathbf{a})$ , with  $\mathbf{a}$  the position of anchor point on the substrate and  $\mathbf{h}$  the position of the motor head. Bound motor heads are modeled as moving continuously along a protofilament with a velocity of  $v_m$ . Because of thermodynamic limits to motor power [79], the motor speed decreases linearly with the tangential component of the motor force  $f^T$  against the movement:

$$v_m = v_0 \left(1 - \frac{f^T}{f_s}\right), \quad (5)$$

where  $v_0$  is the motor unloaded speed, and  $f_s$  is its stall force.

When the stiffness  $k_m$  is sufficient, this movement propels the filament forward, allowing it to glide across the substrate.

Bound motor heads can detach from the filaments with an off-rate  $\omega_{off}$ , that increases with the motor load,

$$\omega_{off} = \omega_d \exp(\|\mathbf{f}\|/f_d) \quad (6)$$

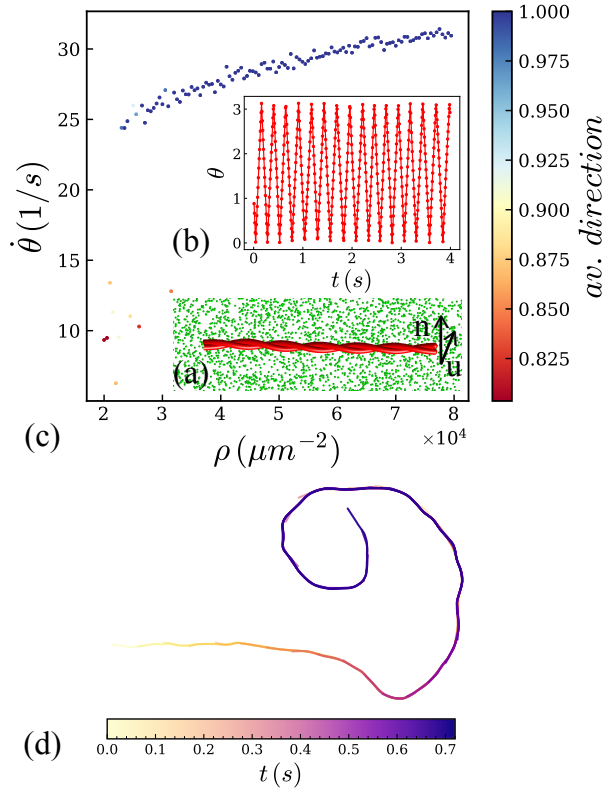


FIG. 5. (a) Schematic illustration of a gliding assay, with anchored motor proteins shown in green. The surface normal is denoted by  $\mathbf{n}$ , and  $\mathbf{u}$  represents the radial unit vector of the helix directed from one protofilament to the other. (b) Sinusoidal variation of the rotational angle,  $\mathbf{n} \cdot \mathbf{u}$ , of the gliding filament as a function of time. (c) Dependence of the angular velocity,  $\dot{\theta}$ , of the gliding filament on motor density. The filament consistently rotates counterclockwise relative to its translational axis, from the barbed (+) end to the pointed (-) end. (d) Time trajectory of a long helical filament (2  $\mu\text{m}$ ) in the gliding assay, showing a counter-clockwise pattern.

where  $\omega_d$  is a constant detachment rate and  $f_d$  is a characteristic detachment force.

The motor parameters are listed in Table S. 1 provided in the Supporting Information, and were chosen to lie within experimentally observed ranges. To reduce computational cost, periodic boundary conditions are applied, whereby the filament exiting one side of the simulation box re-enters from the opposite side. The supplementary Movie S1 shows a helical filament gliding over a surface of motors while simultaneously rotating around its axis. To quantify the filament's chirality, we track a radial unit vector  $\mathbf{u}$  connecting one protofilament to another. The angle between this vector and the surface normal  $\hat{\mathbf{n}}$  varies sinusoidally over time (Fig. 5-b), reflecting the regulation of the rotational motion. Moreover, the rotation rate  $\dot{\theta}$ , increases with motor density. The direction of rotation is determined by the cross product of the radial vector at two consecutive time steps,  $\mathbf{u}(t) \times \mathbf{u}(t+dt)$ .

As shown in Fig. 5-c, the rotation is consistently counterclockwise (indicated by +1 or dark blue) relative to the helical axis, from the minus to the plus end (the opposite direction of translational motion). In our model, motors are assumed to follow the native right-handed chirality of actin, as observed for myosin VI, which results in a counterclockwise rotation relative to the direction of translation (from the plus to the minus end). By contrast, motors such as myosin II, V, and X, which twirl in a left-handed manner around actin filaments, would drive clockwise rotation during gliding, as observed experimentally [52]. In our framework, such left-handed motor activity could be mimicked by imposing a left-handed helicity on the filaments. For an actin filament, the pitch is much larger than the radius ( $P \gg R$ , with  $P/R \sim 10$ ), the translational motion dominates, and rotation appears as a secondary mode. We wondered if chirality could play a larger roles in other situations.

Recent experimental work performed a gliding assay using plant myosin XI, [80], a plus-end directed motor [81]. Instead of going straight, filaments driven by myosin XI take curved trajectories, and the authors observed that these were counter-clockwise. We wondered why we did not observe such movement in our simulations, and hypothesize that our filaments were too short to bend, leading to straight trajectories. In the experiments, the authors used long filaments ( $L \approx 5\mu m$ ), that are easier to bend - since the buckling force scales as  $L_p/L^2$  for a filament gliding on a bed of motors [82]. In addition myosin XI is a fast motor [80, 81], making filament buckling by drag forces likely. We therefore performed additional simulations of long ( $L = 2\mu m$ ) helical actin filaments on a bed of motors. We found that they indeed underwent curved, counter-clockwise trajectories as observed experimentally, Fig. 5-d.

## 2. spiral assay

To better understand the origin of this chiral rotation, we decided to suppress rotational dynamics by fixing in place the minus end of the filament while sitting the filament on a patch of molecular motors. Like in a traditional gliding assay, motors propel the filament ; however, because the minus end is anchored, this leads to filament buckling. Because the anchored end is allowed to freely rotate around its axis, filaments tend to rotate around their minus ends, and we call this setup a *spiral assay*. Anchoring the minus end (called pointed end) of actin filaments can indeed be achieved experimentally [83].

We quantified the direction of rotation by tracking the filament's local orientation vector  $\mathbf{t}_i$  at an arbitrary point  $i$ , and computing the time derivative of the cross product  $\dot{\mathbf{h}} = \mathbf{t}_i(t) \times \mathbf{t}_i(t + \Delta t)/\Delta t$ . We averaged  $\dot{\mathbf{h}}$  over time to compute an average rotation direction, allowing us to compare the behavior of both linear (non-helical) filaments and helical filaments, of similar properties, Fig. 7.

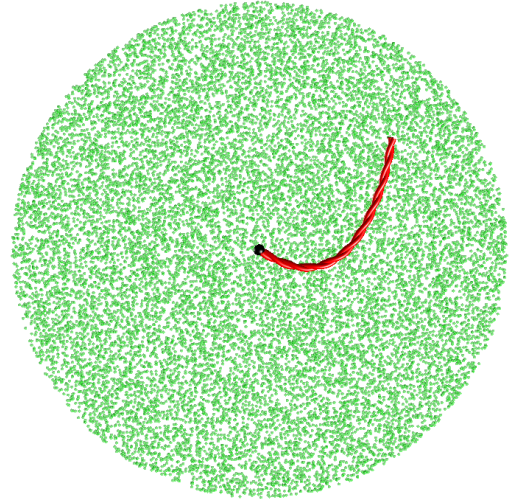


FIG. 6. Schematic representation of a spiral assay in which the minus end of the filament is fixed in space (black dot) to prevent translational motion, while still allowing axial rotation. Anchored motor proteins are shown in green.

We varied systematically the detachment rate,  $\omega_d$ , and detachment force,  $f_d$ , performing 22500 simulations for both type of filament, and computed the average of  $\dot{\mathbf{h}}$  to get the rotation direction. As previously published for linear filaments [82], the phase diagram shows three distinct regimes (Fig. 7-a and Supplementary Movie S2).

For large detachment rates  $\omega_d \gg 1$ , or very small detachment forces  $f_d \simeq 0$ , motors detach rapidly from the filament ( $\omega_{off} \gg 1$ ), preventing them from applying sufficient force to bend it. This regime is labeled as Fluctuation (F), where the filament merely jiggles without any substantial bending. Conversely, at low  $\omega_d$  and high  $f_d$ , the filament exhibits continuous 'beating' (B), during which it rotates in one direction and then switches to another. In between these two regimes, the system shows a continuous 'rotation' (R), where the filament rotates persistently in one direction with little to no switching.

To reduce the stochasticity of the individual results in the total phase diagram, we averaged individual simulation results with neighboring simulations (close in the  $f_d, \omega_d$  parameter space). As expected, linear filaments do not follow a preferred direction, and their rotational direction is random, Fig. 7-c.

Simulating a helical filament in a spiral assay, we find the same three regimes, but very few simulations now show a counter-clockwise (+1/dark blue) rotation, Fig. 7-b. Averaging over neighboring points reveals that the helical filament predominantly rotates in a clockwise direction, consistent with its right-handed structure, Fig. 7-d. Therefore, actin helicity and chirality can bias the large-scale movement of actin filaments. This could contribute to the large-scale chiral patterns that have been

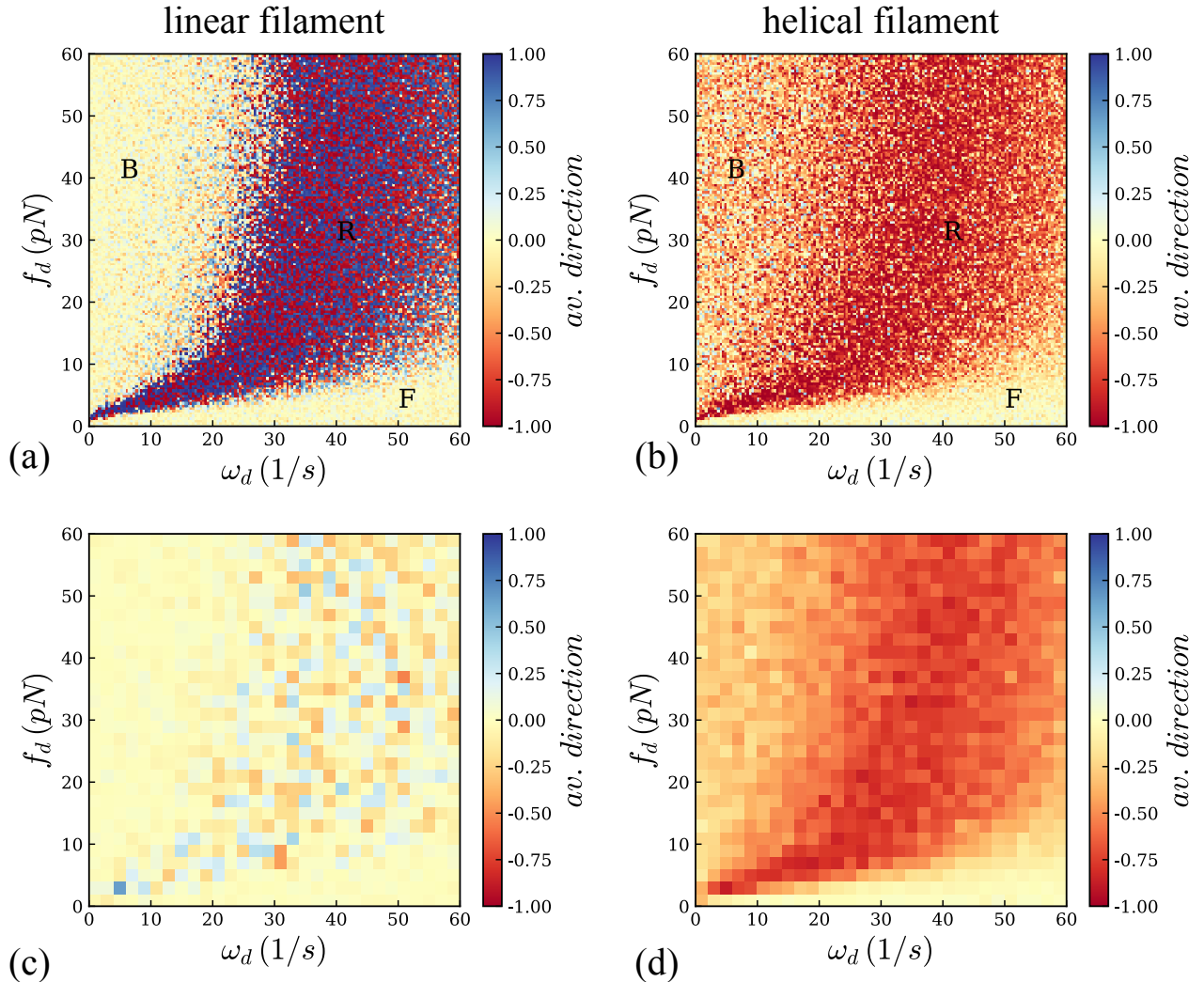


FIG. 7. Phase diagrams of linear (left) and helical (right) filaments in a spiral assay. (a) Results of individual simulations for a linear filament as a function of motor detachment rate ( $\omega_d$ ) and detachment force ( $f_d$ ). Each point corresponds to a single simulation, with colors indicating the average rotation direction of the filament over time. Dark red ( $-1$ ) denotes clockwise rotation, while dark blue ( $+1$ ) indicates counterclockwise motion. Intermediate colors represent cases in which the filament direction has changed over time. Three distinct regimes emerge: fluctuation (F), beating (B), and rotation (R). (b) Corresponding phase diagram for a helical filament with the same persistence length as the linear filament. (c) Averaging individual simulations with their neighboring points reveals no preferred rotation direction for the linear filament. (d) The same averaging procedure for the helical filament shows a tendency for clockwise rotation.

observed for actin in some cells on a substrate [61].

### 3. bundles of helical filaments

So far, we have focused on isolated helical filaments, whereas in nature actin filaments typically assemble into bundles or networks. In-vitro, assemblies of actin filaments and motors were shown to exhibit spontaneous beating motion. In-vivo, thin protrusions called filopodia, made of an actin bundle wrapped in membrane, were shown to exhibit chiral rotation and coiling [63, 84]. To assess the role of actin chirality in such assemblies and

also to demonstrate the computational capability of our model, we considered a bundle composed of 37 helical filaments, arranged in three concentric layers around a central filament, with uniform inter-filament spacing (Fig. 8-a). We fixed the position and orientation of each filament in the bundle, while allowing free rotation of the filament around its axis.

We then designed dimeric motors composed of two motor heads, as described in the previous section, connected by a Hookean spring of high rigidity. Each motor head moves along the protofilaments from the minus to the plus end, thus following the helical trajectory of each filament. The two motor heads of a dimeric motor were

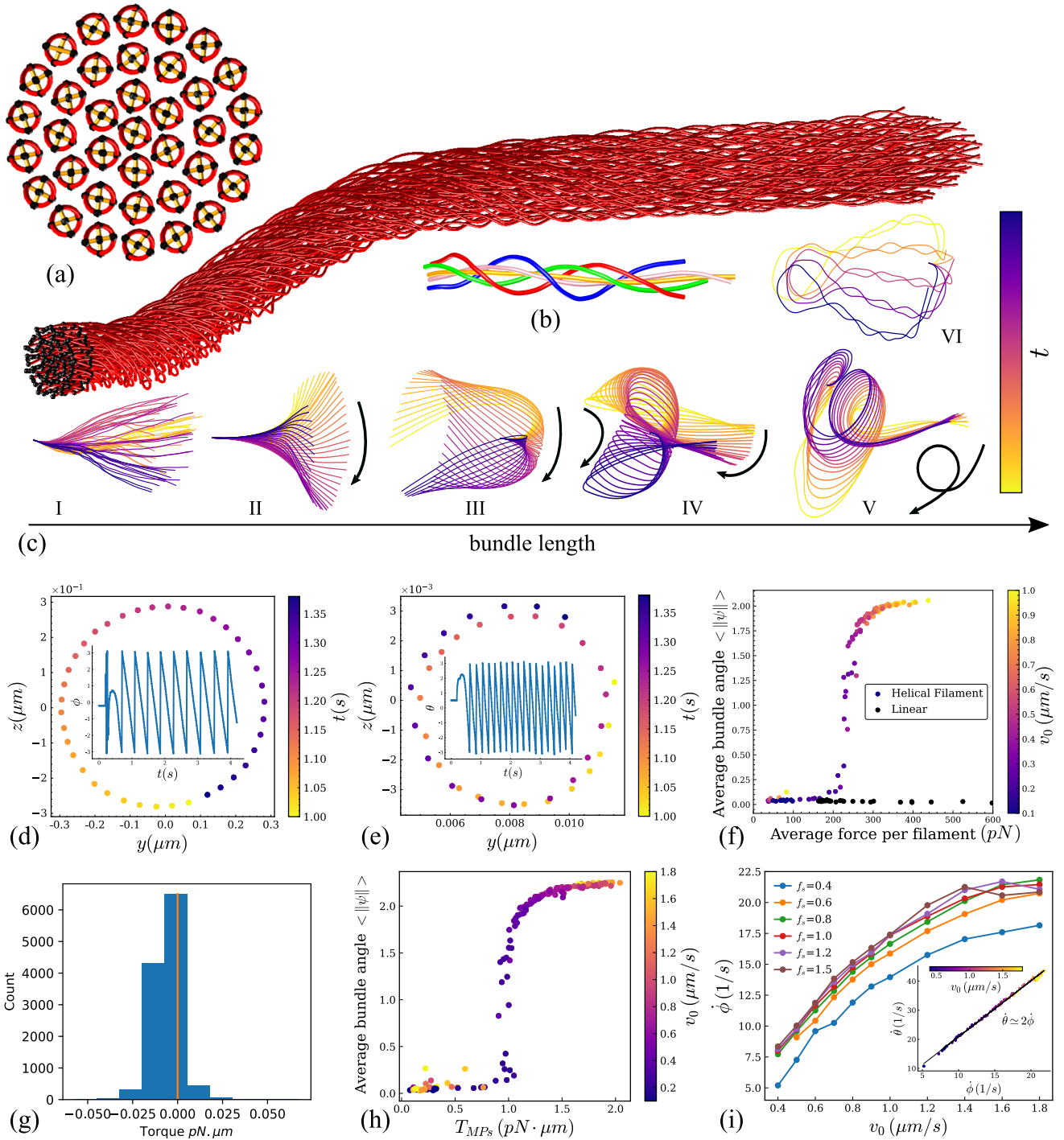


FIG. 8. (a) Snapshot of a bundle consisting of 37 helical filaments arranged in three concentric layers around a central filament. The top panel shows the bundle cross section: the minus ends of the two protofilaments of each helix are connected by a short linear filament, whose center is anchored in space by a pin. This anchoring is repeated twice to fix the bundle both positionally and directionally. (b) Centerlines of four individual helical filaments inside the bundle, each showing helical deformation. (c) Time evolution of the mean bundle axis as a function of bundle length. (d) Time trajectory of the bundle tip, revealing a clockwise rotation. Inset: time evolution of the azimuthal angle,  $\phi$ , of the tip projected onto the  $y-z$  plane. (e) Dynamics of the minus end of a protofilament in a single helix, showing that the filament spins clockwise around its axis with a rotational speed,  $\theta$ , approximately twice that of the bundle tip. Inset: time course of  $\theta$ . (f) Average bundle angle as a function of the average force per filament. (g) Histogram of torque values for 11692 motors for a typical simulation. 20% are positive (counter-clockwise) and 80% are negative (clockwise). (h) Variation of bundle curvature angle,  $\psi$ , as a function of accumulated torque in a bundle of length  $1, \mu m$ , showing a sharp transition. Colors correspond to different motor unloaded speeds. (i) Dependence of bundle azimuthal rotation speed,  $\dot{\phi}$ , on motor unloaded speed  $v_0$  for a bundle of length  $1, \mu m$ . Inset: Relation between  $\dot{\phi}$  and the helix spinning speed  $\dot{\theta}$ ; both increase with  $v_0$  and are linked by  $\dot{\phi} = 2\dot{\theta}$ .

restricted to binding only protofilaments belonging to different helices. The details of the motor properties for this setup are summarized in Table 1 of the Supporting Information.

We found that even in this minimal setting, we could observe a stationary, large scale clockwise rotation (as viewed from bundle tip towards the bundle stem) of the bundle, Fig. 8-a,d. Concurrently to rotation, the bundle underwent deformation and took a curved shape ; the exact shape of the bundle depends on the filament morphology and motor activity. For short bundles, the bundle exhibits small fluctuations around its direction (Fig. 8-c, Panel I, and supplementary movie S3). As the length increases, the torque induces a global clockwise rotation of the bundle while the tip remains forward-directed (Panel II). With further increases in length, the tip bends backward and the bundle develops a noticeable curvature (Panel III). For longer bundles, the curvature increases and the bundle coils toward the anchored end, with the tip rotating clockwise while the coiling itself progresses counterclockwise (Panel IV and supplementary movie S4). At sufficiently large lengths, we observed helical buckling in the bundle (Panel V). In some cases, the bundle becomes supercoiled, with the entire structure rotating in a clockwise direction (Panel VI'). This was reminiscent of the behavior of filopodia, that chirally rotate around their axis and can even coil [63]. It was proposed that this movement and deformation of the filopodia is caused by a nematic instability of the actin-myosin complex. In that model, gradients in filaments orientation lead to active forces. When the system is large enough, this generates spontaneous flows resulting in twist. In this model, movement depends on filament orientation but not on their chirality, that merely selects the rotation direction as an after-effect [63]. While our system is greatly simplified compared to in-vivo filopodia, we decided to investigate whether the deformation and rotation we observed was of nematic or chiral nature. We performed the same simulations with linear filaments instead of helical filaments, and observed neither bundle deformation nor rotation, Fig. 8-f. The rotation we see thus comes from a chiral effect rather than a nematic instability. Indeed, our system is small and may be beneath the threshold for the nematic phase transition. A chiral beating instability is actually expected from chiral bundles with motors even for small discrete bundles such as cilia [85].

We then decided to investigate the origin of these large-scale rotations, focusing on  $1\mu\text{m}$  bundles (Fig. 8-c, panel III). For that, we analyzed the movement and position of the bundle backbone. Starting with a filament initially along the  $Ox$  axis, we described the position of a point  $\mathbf{r} = (\mathbf{x}, \mathbf{y}, \mathbf{z})$  by two angles,  $\psi = \arcsin(\mathbf{t} \cdot \mathbf{x} / \|\mathbf{x}\|)$  and  $\phi$  defined as  $y = \rho \cos \phi$  and  $z = \rho \sin \phi$ , with  $\rho = y^2 + z^2$ . Additionally, we defined  $\theta$  the angle of the interprotofilament vector  $\mathbf{u}$  in the  $Oyz$  plane, taken at the filament minus end. First, we measured the rotation rate  $\dot{\phi}$  of the bundle. We realized that  $\dot{\phi}$  was an increasing

function of both motor unloaded speed  $v_0$  and stall force  $f_s$ , Fig. 8-i, showing that this motion was caused by motor activity, as expected. Because of the helical nature of the filaments, dimeric motor should cause the filaments to rotate, as seen in simulations of gliding assays. Indeed, we could measure the rotation rate  $\dot{\theta}$  of filaments around their axis, and found filaments to rotate at a rate roughly twice the rotation rate  $\dot{\phi}$  of the bundle, Fig. 8-d, and Fig. 8-i, inset. However, it was not clear how this rotation of filaments inside the bundle would lead to rotation of the bundle itself.

Because we could observe rotation in the gliding assay, we know that motors apply a torque on filaments because of their helical nature. For a perfect bundle, it could be possible for all filaments to turn in register, with all motors applying the same torque on filaments. However, defects in the bundle lattice or motor distribution could decrease (resp. increase) the torque on one given filament, decreasing (resp. increasing) its rotation rate, and new defects could appear from the mismatch. This could result in an instability of synchronous rotation pattern of filaments in the bundle, and create an internal friction in the bundle, leading to its deformation and rotation.

By closely monitoring simulation results, we realized that the backbones of individual filaments also undertook a helical shape inside the bundle, Fig. 8-b and supplementary movie S5, and this helix itself rotates around the bundle axis, Fig. 8-f and supplementary movie S6. Therefore, actin bundles were far from ideally aligned, and we expect such mismatch to occur. To test this hypothesis, we quantified the torque motors exerted on filaments. We found that while most motors exert a clockwise torque, a sizeable fraction of motors also apply a counter-clockwise torque, Fig. 8-g. There is therefore indeed defects, or torque mismatches, inside the bundle. We then computed the net torque  $T_{MPS}$  on each filament ; this net torque is clockwise, as expected. Strikingly, we found that there is a critical net torque above which the bundle deforms, Fig. 8-h. Therefore, the bundle deformation and rotation we observe come from a chiral rather than a nematic instability.

#### IV. DISCUSSION

The functionality of actin filaments is strongly linked to their mechanical properties, including helicity and chirality. In this study, we introduced a highly coarse-grained model of actin filaments that enables mesoscale simulations while preserving their helicity and chirality. The framework is implemented in Cytosim, a well-known cytoskeleton simulation software. The model incorporates two geometric parameters—initial radius ( $R_0$ ) and initial pitch ( $P_0$ )—and three microscopic rigidities: bending rigidity ( $\kappa$ ), spring stiffness ( $K$ ), and torque stiffness ( $\Gamma$ ). Due to the interactions within the system, an effective helical structure emerges, characterized by three mechanical properties : the bending persistence

length of the helix ( $L_P$ ), torsional rigidity ( $K_\tau$ ), and inter-protofilament separation rigidity ( $K_S$ ), as well as two geometrical properties : radius  $R$  and pitch  $P$ .

In nature, these macroscopic properties can vary with changes in environmental conditions or interactions with binding proteins. For example, proteins like phalloidin and cofilin can modify the persistence length and pitch of actin filaments. We found that we could predict the geometrical and mechanical properties as a function of the microscopic parameters using simple models consist of springs in series and parallel. This makes it possible to rapidly select adequate parameters to match any given experimental conditions. It also allows our framework to be used for other helical filaments, such as the bacterial cytoskeleton. Here, we provide default parameters for a generic actin filament in table I. The filaments we implemented are also fully integrated into the cytosim platform, allowing us to model their growth dynamic, or to let them interact with molecular motors.

For motors moving along a single filament, we could expect chirality to arise in motor-driven dynamics. To investigate this, we first examined helical filaments in a gliding assay with anchored motor proteins, designed to step directionally from the filament's minus end toward its plus end. Owing to the intrinsic right-handed helicity of actin, the filaments consistently exhibited chiral spinning in addition to their translational motion, with both rotational and translational speeds increasing with motor density. For longer filaments, we observed counter-clockwise curved trajectories as observed experimentally.

In the second setup, a spiral assay, the minus end of the filament was fixed, suppressing translational motion while still allowing axial spinning. Anchored motors can exert forces on the filament, leading to its bending. Under these conditions, three distinct regimes emerged depending on motor properties: fluctuation, rotation, and beating, as previously found for non-helical actin filaments [82]. Here, we find the same three behaviors, but actin chirality impose a clockwise motion. The spiral filament shape we observed for filaments on a motor-covered surface was reminiscent of the shape of actin bundles at the cell surface observed in-vivo [61]. In that study, formin was proposed to be the main contributor to chirality, but motors were shown to be responsible for cable movement, and therefore could play a role in the chirality itself.

Indeed, in many natural and cellular contexts, actin filaments typically assemble into bundles or networks, that can exhibit large-scale chirality. We therefore assessed the role of actin chirality in a bundle of helical filaments connected by dimeric motors. As the motors follow the filament's helicity, they exert torques on the

filaments. We found that torque is not evenly distributed among all motors, causing defects in the whole structure that led to the deformation and rotation of the bundle. This rotation is intrinsically clockwise when viewed from the filament tip toward the anchored minus ends. Depending on bundle length and motor activity, the system exhibited distinct configurations, including rotation, coiling, and helical buckling, reminiscent of those observed in filopodia, an actin-rich cellular structure. Interestingly, in our simulations, the rotation onset corresponds to a chiral instability rather than a nematic one. In filopodia, motion is driven by myosins V and X, that are left handed because of their discrete stepping motion between protofilaments [52]. Our framework allows for the modeling of such motors in the future, that should lead to counterclockwise rotation as observed experimentally.

Overall we found that chiral motion generated by motors interacting with chiral filaments lead to chiral bundle motion. We expect this to be a general feature and to be independent on the details of motor motion, or the exact nature of the filament chirality. Indeed, in near 2D-setups, bundles of actin filaments connected by motors have been found to beat [86]. This chiral instability should also apply to microtubule, on which dynein walks helically [87]. Indeed previous theoretical work on cilia showed that twist exerted by motors in the microtubule bundle generated chiral beating of the cilia [85]. Moreover, motor-bound bundles of microtubulules were also shown experimentally to exhibit a beating behaviour [88]. Chiral beating can induce fluid flows [85]. This could explain why several forms of cilia and flagella evolved convergently [89], requiring few additional proteins, and leading to fluid flows, allowing for various biological functions, including cellular motion or food collection.

## V. ACKNOWLEDGEMENTS

The authors would like to thank Nicolas Minc, Antoine Jégou, Wouter Kools, Guillaume Romet-Lemonne for scientific discussions. We gratefully acknowledge Joel Marchand for the IT support and the IPOP-UP computing cluster. A.Kh. and S.D. would like to thank the INSERM Aviesan grant "MMINOS" and Université Paris Cité's Émergence program for financial support. F.N. gratefully acknowledges support from the European Research Council (ERC Synergy Grant, project 951430).

## VI. DATA ACCESSIBILITY

All code used in this work will be publicly released upon publication.

---

[1] H. Lodish, A. Berk, L. Zipursky, P. Matsudaira, D. Baltimore, and J. Darnell, *Molecular Cell Biology*, 4th ed.

(W. H. Freeman, 2000).

[2] P. Sheterline, J. Clayton, and J. C. Sparrow, *Actin* (OUP Oxford, 1999).

[3] J. Pfaendtner, E. Lyman, T. D. Pollard, and G. A. Voth, Structure and dynamics of the actin filament, *Journal of molecular biology* **396**, 252 (2010).

[4] W. Kabsch and J. Vandekerckhove, Structure and function of actin, *Annual review of biophysics and biomolecular structure* **21**, 49 (1992).

[5] J. R. Bamburg and P. W. O'Neil, Adf/cofilin and actin dynamics in disease, *Trends in cell biology* **12**, 598 (2002).

[6] E. D. Korn, Actin polymerization and its regulation by proteins from nonmuscle cells., *Physiological reviews* **62**, 672 (1982).

[7] J. Tuszyński, J. Brown, and D. Sept, Models of the collective behavior of proteins in cells: tubulin, actin and motor proteins, *Journal of biological physics* **29**, 401 (2003).

[8] R. H. Depue Jr and R. V. Rice, F-actin is a right-handed helix, *Journal of molecular biology* **12**, 302 (1965).

[9] A. Jegou and G. Romet-Lemonne, The many implications of actin filament helicity, in *Seminars in Cell & Developmental Biology*, Vol. 102 (Elsevier, 2020) pp. 65–72.

[10] T. D. Pollard and G. G. Borisy, Cellular motility driven by assembly and disassembly of actin filaments, *Cell* **112**, 453 (2003).

[11] W. Cao, J. P. Goodarzi, and M. Enrique, Energetics and kinetics of cooperative cofilin–actin filament interactions, *Journal of molecular biology* **361**, 257 (2006).

[12] B. R. McCullough, L. Blanchoin, J.-L. Martiel, and M. Enrique, Cofilin increases the bending flexibility of actin filaments: implications for severing and cell mechanics, *Journal of molecular biology* **381**, 550 (2008).

[13] M. A. Deriu, A. Shkurti, G. Paciello, T. C. Bidone, U. Morbiducci, E. Ficarra, A. Audenino, and A. Acquaviva, Multiscale modeling of cellular actin filaments: From atomistic molecular to coarse-grained dynamics, *Proteins: Structure, Function, and Bioinformatics* **80**, 1598 (2012).

[14] S. Panyukov and Y. Rabin, Thermal fluctuations of elastic filaments with spontaneous curvature and torsion, *Physical Review Letters* **85**, 2404 (2000).

[15] S. Panyukov and Y. Rabin, Fluctuating filaments: statistical mechanics of helices, *Physical Review E* **62**, 7135 (2000).

[16] W. Zheng and S. Doniach, A comparative study of motor-protein motions by using a simple elastic-network model, *Proceedings of the National Academy of Sciences* **100**, 13253 (2003).

[17] J. Berro, A. Michelot, L. Blanchoin, D. R. Kovar, and J.-L. Martiel, Attachment conditions control actin filament buckling and the production of forces, *Biophysical journal* **92**, 2546 (2007).

[18] A. De Col and T. B. Liverpool, Statistical mechanics of double-helical polymers, *Physical Review E* **69**, 061907 (2004).

[19] J. Y. Lee, T. M. Iverson, and R. I. Dima, Molecular investigations into the mechanics of actin in different nucleotide states, *The Journal of Physical Chemistry B* **115**, 186 (2011).

[20] J.-W. Chu and G. A. Voth, Allostery of actin filaments: molecular dynamics simulations and coarse-grained analysis, *Proceedings of the National Academy of Sciences* **102**, 13111 (2005).

[21] O. N. Yogurtcu, J. S. Kim, and S. X. Sun, A mechanochemical model of actin filaments, *Biophysical journal* **103**, 719 (2012).

[22] W. Kabsch, H. G. Mannherz, D. Suck, E. F. Pai, and K. C. Holmes, Atomic structure of the actin: Dnase i complex, *Nature* **347**, 37 (1990).

[23] P. Graceffa and R. Dominguez, Crystal structure of monomeric actin in the atp state: structural basis of nucleotide-dependent actin dynamics, *Journal of Biological Chemistry* **278**, 34172 (2003).

[24] J. Pfaendtner, E. M. De La Cruz, and G. A. Voth, Actin filament remodeling by actin depolymerization factor/cofilin, *Proceedings of the National Academy of Sciences* **107**, 7299 (2010).

[25] J.-W. Chu and G. A. Voth, Coarse-grained modeling of the actin filament derived from atomistic-scale simulations, *Biophysical journal* **90**, 1572 (2006).

[26] D. Ming, Y. Kong, Y. Wu, and J. Ma, Simulation of f-actin filaments of several microns, *Biophysical journal* **85**, 27 (2003).

[27] D. Sept and J. A. McCammon, Thermodynamics and kinetics of actin filament nucleation, *Biophysical journal* **81**, 667 (2001).

[28] X. Yu and A. Carlsson, Kinetics of filament bundling with attractive interactions, *Biophysical journal* **87**, 3679 (2004).

[29] A. Carlsson, Stimulation of actin polymerization by filament severing, *Biophysical journal* **90**, 413 (2006).

[30] X. Yu and A. Carlsson, Multiscale study of counterion-induced attraction and bundle formation of f-actin using an ising-like mean-field model, *Biophysical journal* **85**, 3532 (2003).

[31] A. R. Atilgan, S. Durell, R. L. Jernigan, M. C. Demirel, O. Keskin, and I. Bahar, Anisotropy of fluctuation dynamics of proteins with an elastic network model, *Biophysical journal* **80**, 505 (2001).

[32] D. ben Avraham and M. M. Tirion, Dynamic and elastic properties of f-actin: a normal-modes analysis, *Biophysical journal* **68**, 1231 (1995).

[33] G. Ayton and G. Voth, Bridged microscopic and mesoscopic computer simulations for biological systems, in *BIOPHYSICAL JOURNAL*, Vol. 84 (BIOPHYSICAL SOCIETY 9650 ROCKVILLE PIKE, BETHESDA, MD 20814-3998 USA, 2003) pp. 465A–466A.

[34] S. J. Marrink and A. E. Mark, Molecular dynamics simulation of the formation, structure, and dynamics of small phospholipid vesicles, *Journal of the American Chemical Society* **125**, 15233 (2003).

[35] A. Khosravanzadeh, P. Sens, and F. Mohammad-Rafiee, Wrapping of a nanowire by a supported lipid membrane, *Soft matter* **15**, 7490 (2019).

[36] A. Khosravanzadeh, P. Sens, and F. Mohammad-Rafiee, Role of particle local curvature in cellular wrapping, *Journal of the Royal Society Interface* **19**, 20220462 (2022).

[37] F. Nedelec and D. Foethke, Collective langevin dynamics of flexible cytoskeletal fibers, *New Journal of Physics* **9**, 427 (2007).

[38] K. Popov, J. Komianos, and G. A. Papoian, Medyan: mechanochemical simulations of contraction and polarity alignment in actomyosin networks, *PLoS computational biology* **12**, e1004877 (2016).

[39] O. Maxian, R. P. Peláez, A. Mogilner, and A. Donev, Simulations of dynamically cross-linked actin networks:

morphology, rheology, and hydrodynamic interactions, *PLoS computational biology* **17**, e1009240 (2021).

[40] W. Yan, S. Ansari, A. Lamson, M. A. Glaser, R. Blackwell, M. D. Betterton, and M. Shelley, Toward the cellular-scale simulation of motor-driven cytoskeletal assemblies, *Elife* **11**, e74160 (2022).

[41] H. Isambert, P. Venier, A. C. Maggs, A. Fattoum, R. Kassab, D. Pantaloni, and M.-F. Carlier, Flexibility of actin filaments derived from thermal fluctuations: effect of bound nucleotide, phalloidin, and muscle regulatory proteins, *Journal of Biological Chemistry* **270**, 11437 (1995).

[42] C. P. Brangwynne, G. H. Koenderink, E. Barry, Z. Dogic, F. C. MacKintosh, and D. A. Weitz, Bending dynamics of fluctuating biopolymers probed by automated high-resolution filament tracking, *Biophysical journal* **93**, 346 (2007).

[43] A. Ott, M. Magnasco, A. Simon, and A. Libchaber, Measurement of the persistence length of polymerized actin using fluorescence microscopy, *Physical Review E* **48**, R1642 (1993).

[44] H. Kojima, A. Ishijima, and T. Yanagida, Direct measurement of stiffness of single actin filaments with and without tropomyosin by in vitro nanomanipulation., *Proceedings of the National Academy of Sciences* **91**, 12962 (1994).

[45] P. A. Janmey, S. Hvidt, G. F. Oster, J. Lamb, T. P. Stossel, and J. H. Hartwig, Effect of atp on actin filament stiffness, *Nature* **347**, 95 (1990).

[46] Y. Tsuda, H. Yasutake, A. Ishijima, and T. Yanagida, Torsional rigidity of single actin filaments and actin–actin bond breaking force under torsion measured directly by in vitro micromanipulation, *Proceedings of the National Academy of Sciences* **93**, 12937 (1996).

[47] R. Yasuda, H. Miyata, and K. Kinosita Jr, Direct measurement of the torsional rigidity of single actin filaments, *Journal of molecular biology* **263**, 227 (1996).

[48] J. P. Bibeau, N. G. Pandit, S. Gray, N. Shatery Nejad, C. V. Sindelar, W. Cao, and E. M. De La Cruz, Twist response of actin filaments, *Proceedings of the National Academy of Sciences* **120**, e2208536120 (2023).

[49] S. Li, J. Zhang, C. Wang, and P. Nithiarasu, Atomistic modeling of f-actin mechanical responses and determination of mechanical properties, *ACS Biomaterials Science & Engineering* **4**, 2794 (2018).

[50] F. Gittes, B. Mickey, J. Nettleton, and J. , Flexural rigidity of microtubules and actin filaments measured from thermal fluctuations in shape., *The Journal of cell biology* **120**, 923 (1993).

[51] M. A. Hartman and J. A. Spudich, The myosin superfamily at a glance, *Journal of cell science* **125**, 1627 (2012).

[52] M. Y. Ali, S. Uemura, K. Adachi, H. Itoh, K. Kinosita Jr, and S. Ishiwata, Myosin v is a left-handed spiral motor on the right-handed actin helix, *Nature structural biology* **9**, 464 (2002).

[53] I. Sase, H. Miyata, S. Ishiwata, and K. Kinosita Jr, Axial rotation of sliding actin filaments revealed by single-fluorophore imaging, *Proceedings of the National Academy of Sciences* **94**, 5646 (1997).

[54] J. F. Beausang, H. W. Schroeder, P. C. Nelson, and Y. E. Goldman, Twirling of actin by myosins ii and v observed via polarized tif in a modified gliding assay, *Biophysical journal* **95**, 5820 (2008).

[55] A. Vilfan, Twirling motion of actin filaments in gliding assays with nonprocessive myosin motors, *Biophysical journal* **97**, 1130 (2009).

[56] Y. Tanaka, A. Ishijima, and S. Ishiwata, Super helix formation of actin filaments in an in vitro motile system, *Biochimica et Biophysica Acta (BBA)-Protein Structure and Molecular Enzymology* **1159**, 94 (1992).

[57] H. Mizuno, C. Higashida, Y. Yuan, T. Ishizaki, S. Narumiya, and N. Watanabe, Rotational movement of the formin mida1 along the double helical strand of an actin filament, *Science* **331**, 80 (2011).

[58] T. Nishizaka, T. Yagi, Y. Tanaka, and S. Ishiwata, Right-handed rotation of an actin filament in an in vitro motile system, *Nature* **361**, 269 (1993).

[59] T. Sanchez, I. Kulic, and Z. Dogic, Circularization, photomechanical switching, and a supercoiling transition of actin filaments, *Physical review letters* **104**, 098103 (2010).

[60] A. Tamada, S. Kawase, F. Murakami, and H. Kamiguchi, Autonomous right-screw rotation of growth cone filopodia drives neurite turning, *Journal of Cell Biology* **188**, 429 (2010).

[61] Y. H. Tee, T. Shemesh, V. Thiagarajan, R. F. Hariadi, K. L. Anderson, C. Page, N. Volkmann, D. Hanein, S. Sivaramakrishnan, M. M. Kozlov, *et al.*, Cellular chirality arising from the self-organization of the actin cytoskeleton, *Nature cell biology* **17**, 445 (2015).

[62] N. Leijnse, L. B. Oddershede, and P. M. Bendix, Helical buckling of actin inside filopodia generates traction, *Proceedings of the National Academy of Sciences* **112**, 136 (2015).

[63] N. Leijnse, Y. F. Barooji, M. R. Arastoo, S. L. Sønder, B. Verhagen, L. Wullkopf, J. T. Erler, S. Semsey, J. Nylandsted, L. B. Oddershede, *et al.*, Filopodia rotate and coil by actively generating twist in their actin shaft, *Nature Communications* **13**, 1636 (2022).

[64] S. R. Naganathan, S. Fürthauer, M. Nishikawa, F. Jülicher, and S. W. Grill, Active torque generation by the actomyosin cell cortex drives left–right symmetry breaking, *elife* **3**, e04165 (2014).

[65] S. R. Naganathan, T. C. Middelkoop, S. Fürthauer, and S. W. Grill, Actomyosin-driven left-right asymmetry: from molecular torques to chiral self organization, *Current opinion in cell biology* **38**, 24 (2016).

[66] C. A. Lugo, E. Saikia, and F. Nedelec, A typical workflow to simulate cytoskeletal systems with cytosim, *arXiv preprint arXiv:2205.13852* (2022).

[67] T. Strübing, A. Khosravanzadeh, A. Vilfan, E. Boden-schatz, R. Golestanian, and I. Guido, Wrinkling instability in 3d active nematics, *Nano letters* **20**, 6281 (2020).

[68] M. Mund, J. A. van Der Beek, J. Deschamps, S. Dmitrieff, P. Hoess, J. L. Monster, A. Picco, F. Nédélec, M. Kaksonen, and J. Ries, Systematic nanoscale analysis of endocytosis links efficient vesicle formation to patterned actin nucleation, *Cell* **174**, 884 (2018).

[69] W.-X. Chew, G. Henkin, F. Nédélec, and T. Surrey, Effects of microtubule length and crowding on active microtubule network organization, *Iscience* **26**, 106063 (2023).

[70] S. Dmitrieff, A. Alsina, A. Mathur, and F. J. Nédélec, Balance of microtubule stiffness and cortical tension determines the size of blood cells with marginal band across species, *Proceedings of the National Academy of Sciences* **114**, 4418 (2017).

- [71] Y. Liu, T. Pérez, W. Li, J. Gunton, and A. Green, Statistical mechanics of helical wormlike chain model, *The Journal of chemical physics* **134**, 02B622 (2011).
- [72] L. Giomi and L. Mahadevan, Statistical mechanics of developable ribbons, *Physical review letters* **104**, 238104 (2010).
- [73] R. D. Kamien, The geometry of soft materials: a primer, *Reviews of Modern physics* **74**, 953 (2002).
- [74] M. Bathe, C. Heussinger, M. M. Claessens, A. R. Bausch, and E. Frey, Cytoskeletal bundle mechanics, *Biophysical journal* **94**, 2955 (2008).
- [75] S. Harteis and S. Schneider, Making the bend: Dna tertiary structure and protein-dna interactions, *International journal of molecular sciences* **15**, 12335 (2014).
- [76] N. Ma and A. van der Vaart, Anisotropy of b-dna groove bending, *Journal of the American Chemical Society* **138**, 9951 (2016).
- [77] M. L. Gardel, K. E. Kasza, C. P. Brangwynne, J. Liu, and D. A. Weitz, Mechanical response of cytoskeletal networks, *Methods in cell biology* **89**, 487 (2008).
- [78] J. Löwe, F. van den Ent, and L. A. Amos, Molecules of the bacterial cytoskeleton, *Annu. Rev. Biophys. Biomol. Struct.* **33**, 177 (2004).
- [79] J. Howard, Mechanics of motor proteins, in *Physics of bio-molecules and cells. Physique des biomolécules et des cellules: session LXXV. 2–27 July 2001* (Springer, 2002) pp. 69–94.
- [80] T. Haraguchi, K. Yoshimura, Y. Inoue, T. Imi, K. Hasegawa, T. Nagai, T. Mori, K. Matsuno, and K. Ito, Elucidating chiral myosin-induced actin dynamics: From single filament behavior to collective structures, *bioRxiv*, 2025 (2025).
- [81] M. Tominaga, H. Kojima, E. Yokota, H. Orii, R. Nakamori, E. Katayama, M. Anson, T. Shimmen, and K. Oiwa, Higher plant myosin xi moves processively on actin with 35 nm steps at high velocity, *The EMBO journal* (2003).
- [82] A. Khosravanzadeh and S. Dmitrieff, Dynamic clamping induces rotation-to-beating transition of pinned filaments in gliding assays, *Journal of the Royal Society Interface* **22**, 20240859 (2025).
- [83] H. Wioland, E. Suzuki, L. Cao, G. Romet-Lemonne, and A. Jegou, The advantages of microfluidics to study actin biochemistry and biomechanics, *Journal of Muscle Research and Cell Motility* **41**, 175 (2020).
- [84] W. Li, W.-L. Chung, M. M. Kozlov, O. Medalia, B. Geiger, and A. D. Bershadsky, Chiral growth of adherent filopodia, *Biophysical Journal* **122**, 3704 (2023).
- [85] A. Hilfinger and F. Jülicher, The chirality of ciliary beats, *Physical biology* **5**, 016003 (2008).
- [86] M. Pochitaloff, M. Miranda, M. Richard, A. Chaiyasetdhi, Y. Takagi, W. Cao, E. M. De La Cruz, J. R. Sellers, J.-F. Joanny, F. Jülicher, *et al.*, Flagella-like beating of actin bundles driven by self-organized myosin waves, *Nature physics* **18**, 1240 (2022).
- [87] R. D. Vale and Y. Y. Toyoshima, Rotation and translocation of microtubules in vitro induced by dyneins from tetrahymena cilia, *Cell* **52**, 459 (1988).
- [88] T. Sanchez, D. Welch, D. Nicastro, and Z. Dogic, Cilia-like beating of active microtubule bundles, *Science* **333**, 456 (2011).
- [89] D. R. Mitchell, The evolution of eukaryotic cilia and flagella as motile and sensory organelles, *Eukaryotic membranes and cytoskeleton: Origins and evolution* , 130 (2007).

## SUPPORTING INFORMATION

To measure the bending persistence length and torsional rigidity of the helical actin filament, we use two different methods: 1) studying the fluctuation of the single protofilaments by Frenet-Serret frame and a rotation matrix (Fig. S.1-a), 2) studying the fluctuation and mechanical behavior of the whole structure. Each protofilament is a discretized chain of  $N$  segmentation with bond length  $ds$  (Fig. S.2).

At each vertex a local Frenet frame,  $\mathbf{F}_i = (\mathbf{t}_i, \mathbf{n}_i, \mathbf{b}_i)$ , can be constructed by following equations:

$$\mathbf{t}_i = \frac{\mathbf{r}_{i+1} - \mathbf{r}_i}{ds}, \quad \mathbf{b}_i = \frac{\mathbf{t}_{i-1} \times \mathbf{t}_i}{|\mathbf{t}_{i-1} \times \mathbf{t}_i|}, \quad \mathbf{n}_i = \mathbf{b}_i \times \mathbf{t}_i, \quad (7)$$

where  $\mathbf{r}_i$  is the position vector of the vertexes.  $\mathbf{t}_i$ ,  $\mathbf{n}_i$ , and  $\mathbf{b}_i$  are called tangent, normal, and binormal unit vectors, respectively[71–73]. In this formalism, the curvature  $C$  changes to  $C = |\frac{\partial \mathbf{t}(s)}{\partial s}| = (\mathbf{t}_i - \mathbf{t}_{i-1})^2/ds$ . The  $i$ th and  $(i-1)$ th frames can overlap with two consecutive rotations: first, rotation around  $\mathbf{t}_{i-1}$  by the angle  $\phi_i$  and then rotate around  $\mathbf{b}_{i-1}$  by the angle  $\theta_i$ . Therefore, the Frenet frames are related together with a rotation matrix  $\mathbf{F}_i = \mathbf{F}_{i-1} \mathbf{R}_i$ , where  $\mathbf{R}_i$  is made by multiplication of the mentioned rotations.

$$\mathbf{R}_i = \begin{pmatrix} \cos \theta_i & -\sin \theta_i & 0 \\ \sin \theta_i \cos \phi_i & \cos \theta_i \cos \phi_i & -\sin \phi_i \\ \sin \theta_i \sin \phi_i & \cos \theta_i \sin \phi_i & \cos \phi_i \end{pmatrix}. \quad (8)$$

The elements of this matrix can be calculated by following scalar products:

$$\begin{aligned} \cos \theta_i &= \mathbf{t}_i \cdot \mathbf{t}_{i-1}; & \sin \theta_i \cos \phi_i &= \mathbf{t}_i \cdot \mathbf{n}_{i-1} \\ \cos \phi_i &= \mathbf{b}_i \cdot \mathbf{b}_{i-1}; & \sin \theta_i \sin \phi_i &= \mathbf{t}_i \cdot \mathbf{b}_{i-1}. \end{aligned} \quad (9)$$

By multiplying the consecutive matrices, it is possible to move from one frame to another one. The first element of the resulting matrix shows the tangent correlation, and the last element represents the binormal correlation.

$$\begin{aligned} \langle \mathbf{t}_N \cdot \mathbf{t}_0 \rangle &= \langle \mathbf{R}_1 \mathbf{R}_2 \mathbf{R}_3 \cdots \mathbf{R}_N \rangle_{11} = \langle \mathbf{R} \rangle_{11}^N \\ \langle \mathbf{b}_N \cdot \mathbf{b}_0 \rangle &= \langle \mathbf{R}_1 \mathbf{R}_2 \mathbf{R}_3 \cdots \mathbf{R}_N \rangle_{33} = \langle \mathbf{R} \rangle_{33}^N. \end{aligned} \quad (10)$$

On the other hand, a matrix  $\mathbf{V}$  whose columns consist of eigenvectors of  $\langle \mathbf{R} \rangle$  can be used to diagonalize the rotational matrix and determine its eigenvalues

$$\langle \mathbf{R} \rangle^N = \mathbf{V}^{-1} \begin{pmatrix} \lambda_1^N & & \\ & \lambda_2^N & \\ & & \lambda_3^N \end{pmatrix} \mathbf{V} \quad (11)$$

The elements of  $\langle \mathbf{R} \rangle^N$  are the linear combination of  $\lambda_1^N$ ,  $\lambda_2^N$ , and  $\lambda_3^N$ , and the correlation functions can be

written as

$$\begin{aligned} \langle \mathbf{t}_N \cdot \mathbf{t}_0 \rangle &= A_t e^{-\frac{N}{L_P}} + B_t e^{-\frac{N}{L_\tau}} \cos(kN) \\ \langle \mathbf{b}_N \cdot \mathbf{b}_0 \rangle &= A_b e^{-\frac{N}{L_P}} + B_b e^{-\frac{N}{L_\tau}} \cos(kN), \end{aligned} \quad (12)$$

where  $L_P$  and  $L_\tau$  are the bending and torsional persistence length, respectively. The sinusoidal part represents the helicity of the filaments, and  $k$  is the wave number that corresponds to the helix pitch through  $k = 1/\sqrt{R^2 + P^2}$ .  $A_t$ ,  $B_t$ ,  $A_b$ , and  $B_b$  are independent coefficients of  $N$ , and they should satisfy the following relations

$$A_t + B_t = 1; \quad A_b + B_b = 1. \quad (13)$$

More details of the calculations can be found in Ref. [71]. By fitting the eqs. 12 to the simulation results, the bending and torsional persistence length can be measured as shown in Fig. S.1 b and c. The persistence lengths are related to the decaying parts of eqs. 12.

In the second method to measure the bending persistence length of the helical actin filament, we define a hypothetical backbone by averaging the coordinates of the two protofilaments at each contour position (dashed blue line in Fig. S.2-b). The backbone is defined as a linear structure, and the bending persistence length,  $L_P$ , can be obtained from the tangent–tangent correlation function:

$$\langle \mathbf{t}_i \cdot \mathbf{t}_{i+s} \rangle = e^{-s/L_P}, \quad (14)$$

where  $s$  is the contour length along the backbone and  $\mathbf{t}_i$  denotes the unit tangent vector at position  $i$ . A typical measurement of this method is represented in Fig. S.2-a.

We also measured the torsional rigidity of the helical filament using a mechanical approach inspired by experiments [46, 48]. In these studies, one end of an actin filament is fixed to a coverslip to constrain both its position and orientation, while the other end is attached to a bead containing fluorescent markers. Holding the bead in an optical trap suppresses bending, and torsional rigidity can be extracted from its rotational diffusion. More recently, magnetic tweezers have been used to apply direct torque to the bead and measure the resulting twist [48]. Following this principle, we applied two equal and opposite torques to the free ends of the helical filament (corresponding to four forces at the protofilaments ends). To prevent bending during twisting, the ends were coupled by two rigid filaments with their midpoints fixed in space (black lines in Fig. S.2-b). As shown in Fig. S.2-c, the rotation response is linear for small applied torques. The torsional rigidity was therefore calculated from the torque–twist relation:

$$K_\tau = \frac{Tl_0}{\Delta\gamma}, \quad (15)$$

where  $T$  is the applied torque,  $l_0$  the filament's initial length, and  $\Delta\gamma$  the resulting azimuthal rotation angle.

Fig. 3 represents the behavior of the bending persistence length,  $L_P$ , and torsional rigidity,  $K_\tau$ , as a function of spring stiffness,  $K$ , torque stiffness,  $\Gamma$ , and bending rigidity of the protofilaments,  $\kappa$ .

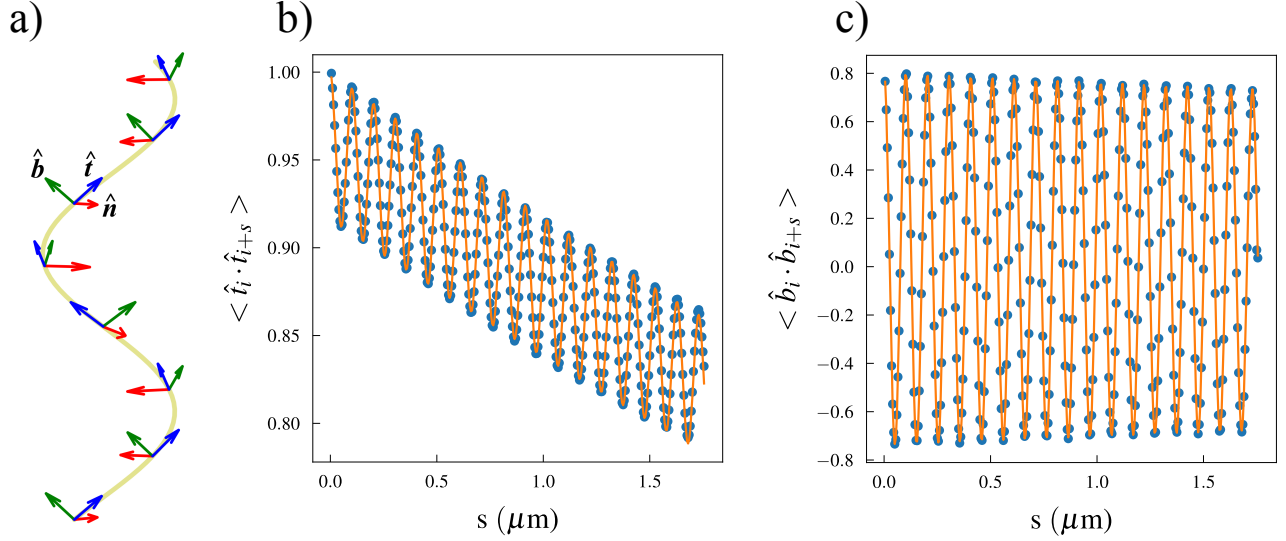


FIG. S.1. Using Frenet frame and rotational matrix to measure the bending and torsional persistence length. a) A Frenet-Serret frame at each point of an individual protofilament is made by three orthogonal vectors: tangent vector ( $\hat{t}$ ), normal vector ( $\hat{n}$ ), and binormal vector ( $\hat{b}$ ). Tangent (b) and binormal (c) correlation functions are related to the bending and torsional persistence lengths by eq. 12.

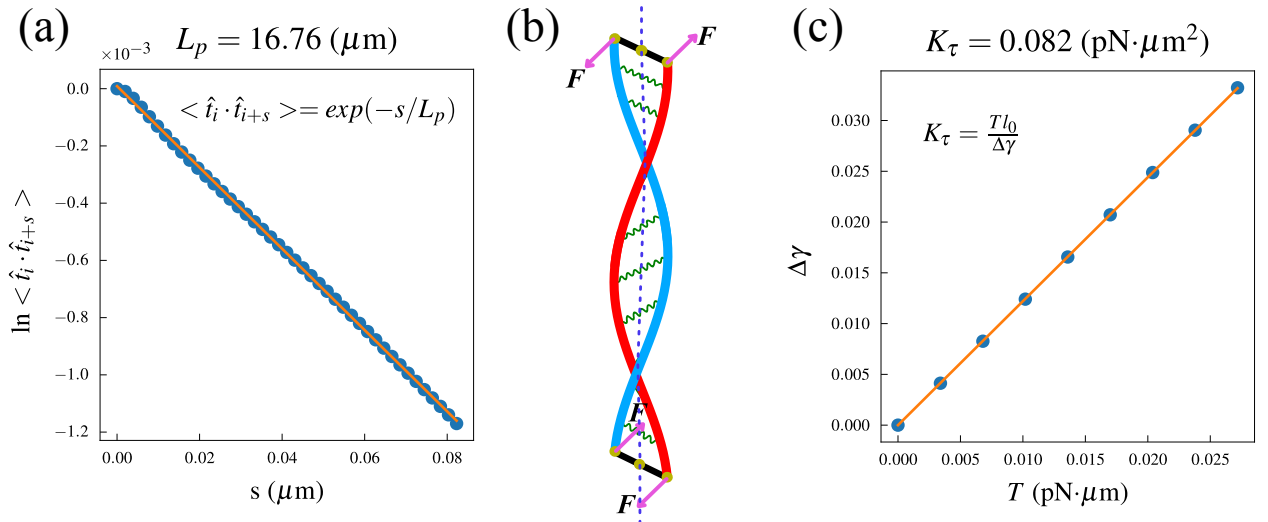


FIG. S.2. (a) Tangent correlation function of the hypothetical axial backbone of the helical filament (dashed line in panel b), used to determine the bending persistence length. (b) Schematic of the setup for measuring the torsional rigidity of the filament, where torque is applied to the free ends of the protofilaments. (c) The torsional angle varies linearly with the applied torque, from which the torsional rigidity of the helix is obtained.

Symbol	Parameter	value	value	value
$k_B T$	Thermal energy	$4.2 \text{ pNm}$	$4.2 \text{ pNm}$	$4.2 \text{ pNm}$
$\Delta t$	Time step	$10^{-4} \text{ s}$	$5 \times 10^{-6} \text{ s}$	$10^{-4} \text{ s}$
$\eta$	Viscosity	$10^{-4} \text{ pN}/\mu\text{m}^2 \text{ s}$	$10^{-4} \text{ pN}/\mu\text{m}^2 \text{ s}$	$5 \times 10^{-5} \text{ pN}/\mu\text{m}^2 \text{ s}$
<b>Filaments</b>				
L	Protofilaments length	$0.3 \mu\text{m}$	$0.4 \mu\text{m}$	$1 \mu\text{m}$ (for Fig. 9-i) $[0.1 - 4] \mu\text{m}$ (for Fig. 9-c)
$\kappa$	Protofilaments bending rigidity	$0.02 \text{ pN} \cdot \mu\text{m}^2$	$0.02 \text{ pN} \cdot \mu\text{m}^2$	$0.02 \text{ pN} \cdot \mu\text{m}^2$
K	Spring stiffness	$10000 \text{ pN}/\mu\text{m}$	$10000 \text{ pN}/\mu\text{m}$	$10000 \text{ pN}/\mu\text{m}$
$\Gamma$	Torque	$7 \text{ pN} \cdot \mu\text{m}$	$7 \text{ pN} \cdot \mu\text{m}$	$7 \text{ pN} \cdot \mu\text{m}$
$R_0$	Initial radius	$3 \text{ nm}$	$3 \text{ nm}$	$3 \text{ nm}$
$P_0$	Initial Pitch	$72 \text{ nm}$	$72 \text{ nm}$	$72 \text{ nm}$
ds	Segmentation length	$2 \text{ nm}$	$2 \text{ nm}$	$5 \text{ nm}$
$\epsilon$	Steric stiffness	-	-	$10000 \text{ pN}/\mu\text{m}$
$r_s$	Steric radius	-	-	$2.5 \text{ nm}$
<b>Motors</b>				
$\omega_{on}$	Binding rate	$200 \text{ s}^{-1}$	$25 \text{ s}^{-1}$	$30 \text{ s}^{-1}$
$r_b$	Binding range	$2 \text{ nm}$	$2 \text{ nm}$	$5 \text{ nm}$
$\omega_d$	detachment rate	$0.3 \text{ s}^{-1}$	$[0.1 - 60] \text{ s}^{-1}$	$1 \text{ s}^{-1}$
$f_d$	Unbinding force	$25 \text{ pN}$	$[0.1 - 60] \text{ pN}$	$10 \text{ pN}$
$f_s$	Stall force	$6 \text{ pN}$	$6 \text{ pN}$	$5 \text{ pN}$
$v_0$	Unloaded speed	$0.5 \mu\text{m}/\text{s}$	$3 \mu\text{m}/\text{s}$	$1 \mu\text{m}/\text{s}$
$k_m$	Spring stiffness	$5000 \text{ pN}/\mu\text{m}$	$500 \text{ pN}/\mu\text{m}$	$500 \text{ pN}/\mu\text{m}$
$\rho_m$	Motor density	$[2 - 8] \times 10^4 \mu\text{m}^{-2}$	$3 \times 10^4 \mu\text{m}^{-2}$	$14.2 \times 10^4 \mu\text{m}^{-3}$

TABLE S.1. Simulation parameters.